

MATERIALS SCIENCE

Pressure-driven fusion of amorphous particles into integrated monoliths

HPSTAR
1201-2021

Zhao Mu^{1†}, Kangren Kong^{1†}, Kai Jiang², Hongliang Dong^{3,4}, Xurong Xu⁵, Zhaoming Liu^{1*}, Ruikang Tang^{1,6*}

Biological organisms can use amorphous precursors to produce inorganic skeletons with continuous structures through complete particle fusion. Synthesizing monoliths is much more difficult because sintering techniques can destroy continuity and limit mechanical strength. We manufactured inorganic monoliths of amorphous calcium carbonate by the fusion of particles while regulating structurally bound water and external pressure. Our monoliths are transparent, owing to their structural continuity, with a mechanical strength approaching that of single-crystal calcite. Dynamic water channels within the amorphous bulk are synergistically controlled by water content and applied pressure and promote mass transportation for particle fusion. Our strategy provides an alternative to traditional sintering methods that should be attractive for constructing monoliths of temperature-sensitive biominerals and biomaterials.

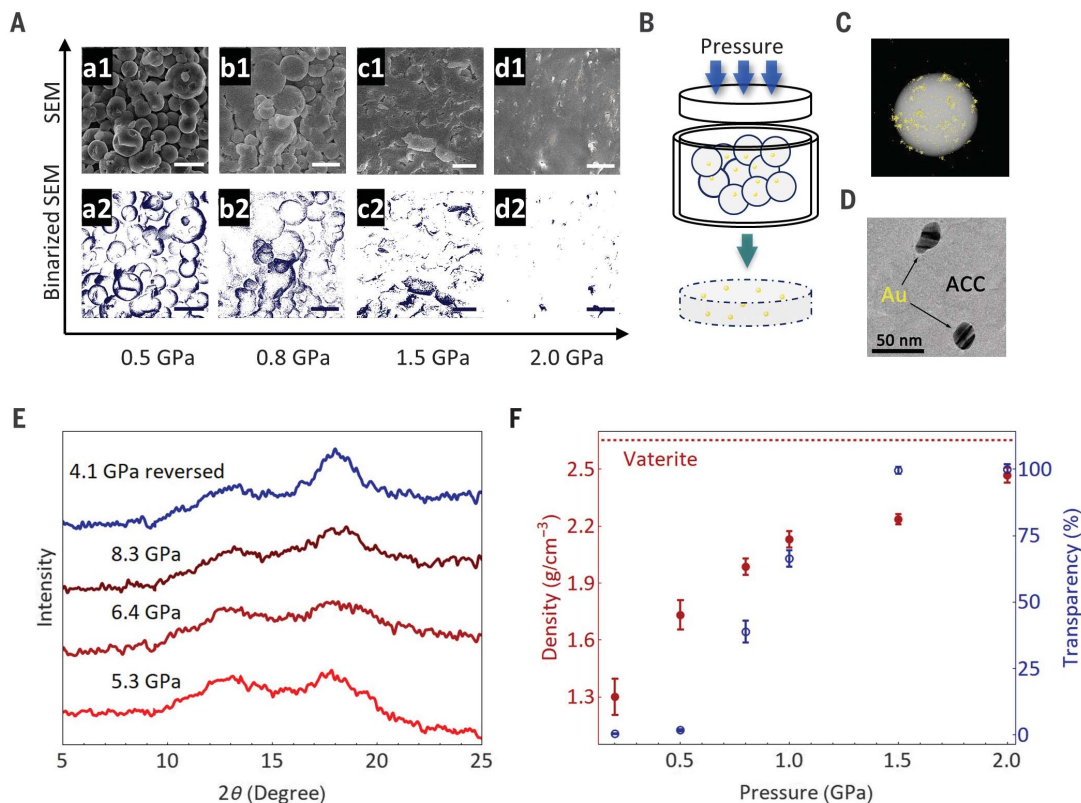
Inorganic materials, especially minerals and ceramics, play important roles in modern society (1–4), but the manufacture of their monoliths is a great challenge (5). In practice, many inorganic materials are produced in powder forms and then consolidated by pressing and sintering (6–10). However, mass transportation among particles is often insufficient through sinter treatment, complete particle-particle fusion cannot be achieved within bulk materials, and particle boundaries remain. Owing to internal discontinuities, the properties of sintered inor-

ganic bulks are not ideal (11, 12), especially with respect to mechanical strength (13). In nature, biological organisms [e.g., sea urchins (14) and coccoliths (15)] can produce inorganic skeletons that have continuous structures with flexible morphology (16). Accordingly, these inorganic skeletons are superior to artificial skeletons because of their structural integration. Increasing evidence has demonstrated that these biological organisms use amorphous particles as precursors to produce skeletons via particle-particle fusion (17–19). Inspired by this biological phenomenon, we suggest that the

manufacture of monolithic inorganic materials can be achieved by fusion of their amorphous precursors under pressure (P). However, many previous attempts using amorphous mineral phases such as amorphous calcium carbonate (ACC) and amorphous calcium phosphate have revealed that external P frequently induces crystallization of amorphous particles rather than particle-particle fusion (20–23). These amorphous mineral phases contain abundant water, which induces dissolution and recrystallization of the intermediate amorphous phases under P .

By controlling the water content (n) within amorphous precursors and the external P , we can achieve biomineralization-like particle fusion, which follows the discovery of pressure-driven mass transportation through dynamic water channels in amorphous phases. By using

¹Department of Chemistry, Zhejiang University, Hangzhou 310027, China. ²Engineering Research Center of Nanophotonics & Advanced Instrument (Ministry of Education), Department of Materials, East China Normal University, Shanghai 200241, China. ³Center for High Pressure Science and Technology Advanced Research, Shanghai 201203, China. ⁴State Key Laboratory of High Performance Ceramics and Superfine Microstructure, Shanghai Institute of Ceramics, Chinese Academy of Sciences, Shanghai 200050, China. ⁵Qiushi Academy for Advanced Studies, Zhejiang University, Hangzhou 310027, China. ⁶State Key Laboratory of Silicon Materials, Zhejiang University, Hangzhou 310027, China. *Corresponding author. Email: oldliu@zju.edu.cn (Z.L.); rtang@zju.edu.cn (R.T.) †These authors contributed equally to this work.



ACC as a typical amorphous precursor, we experimentally demonstrated this control of complete fusion of ACC particles to result in a transparent calcium carbonate monolith. The monolith exhibits optimal mechanical strength with a hardness (H) of 2.739 GPa and a Young's modulus (E) of 49.672 GPa; these values are superior to those of common cement materials and almost reach those of single-crystal calcite (24).

The chemical formula of ACC is $\text{CaCO}_3 \cdot n\text{H}_2\text{O}$, with n frequently being ≥ 1 (20, 25, 26). In our experiments, we synthesized ACC particles with an average size of 450 ± 100 nm (fig. S1) while controlling n between 0 and 1.6 (fig. S2A). We confirmed that ACC particles with $n \geq 1$ cannot coalesce under external P , because phase transformation–based crystallization happens instead (fig. S3), but keeping $n < 1$ enables us to avoid this issue. We used ACC with $n = 0.7$ (fig. S2B) for our typical samples in a subsequent compaction treat-

ment under P . In all of our experiments, the treatment time was 5 min at room temperature. At $P \leq 0.5$ GPa, we did not observe fusion because we could observe the particles and their boundaries under scanning electron microscopy (SEM) (Fig. 1A). When P increased to 0.8 GPa, some ACC particles began to coalesce, but we could still identify their original spherical morphology. The particles further coalesced at a large scale, and the spherical shape disappeared as P increased to 1.5 GPa. At $P = 2.0$ GPa, all ACC particles coalesced completely to form a continuous and uniform bulk. To clearly express the coalescence behavior of ACC particles, we additionally processed their SEM images with binarization (Fig. 1A; blue areas represent non-coalesced particles). The structural discontinuities decreased as P increased from 0.2 to 2.0 GPa, and finally, all individual particles were fused into an integral whole. We used Au nanoparticles to confirm complete coalescence at the nanoscale (Fig. 1B and fig. S4). In this exami-

nation, the ACC particle surfaces were labeled with Au nanoparticles (Fig. 1C). After fusion treatment, these Au particles “moved” from the surface into the interior and were completely surrounded by the uniform ACC phase (Fig. 1D and fig. S5). We verified the surrounding ACC by element mapping (fig. S6) and electron irradiation–induced crystallization (fig. S7). Because we did not observe a gap or pore structure in the Au-labeled monolith, we again confirmed complete particle-particle coalescence.

We performed in situ high-pressure synchrotron radiation x-ray diffraction (XRD) analysis (Fig. 1E) and Fourier transform infrared spectroscopy (fig. S8) to show that the resulting monolith was still ACC and did not undergo crystallization during treatment. This observation is not consistent with previous studies (20, 21). We argue that it follows from our observations that the phase stability of ACC improved as n decreased. During the fusion process, the apparent density (which includes the void volumes) increased, along with the bulk transparency (Fig. 1F). The apparent density of the compacted ACC bulk was ~ 1.30 g/cm³ at 0.2 GPa, and it increased to 2.45 g/cm³ at 2.0 GPa. Because the documented densities of ACC are 1.62 to 2.18 g/cm³ (27–29), the value of 2.45 g/cm³ follows from the formation of a more densified ACC bulk. A comparison of samples before and after the pressure treatment showed that the water content in ACC remained almost unchanged (fig. S2C), which excludes the possibility of water removal from ACC (30). Thus, we attribute the apparent density increase to the elimination of defects and pores by particle-particle fusion. In addition, under the same pressure treatment, the ACC with a lower water content ($n = 0.3$) has a higher apparent density, 2.60 g/cm³. The theoretical density of vaterite, a single crystal of calcium carbonate, is 2.71 g/cm³, and the theoretical density of ACC is in the range of 2.18 to 2.65 g/cm³ (29, 31) at different water contents. This close-packed characteristic follows the continuous internal structure of the resulting ACC monolith.

Microstructural defects in materials commonly cause light scattering, which leads to opacity. The constructed bulk compacted at $P = 0.2$ GPa is white and nontransparent (inset of Fig. 2A), which is due to internal discontinuities (Fig. 1A). When P was increased to 2.0 GPa, the degree of transparency increased substantially, and the constructed bulk became almost transparent (Fig. 1F and inset of Fig. 2A), which indicates that light scattering decreased as a result of improved internal continuity. We used nanoindentation tests to examine the mechanical strengths of the bulks constructed under different P values (Fig. 2A). We calculated E and H using the load-displacement curve. The bulk material constructed at 0.2 GPa performed poorly,

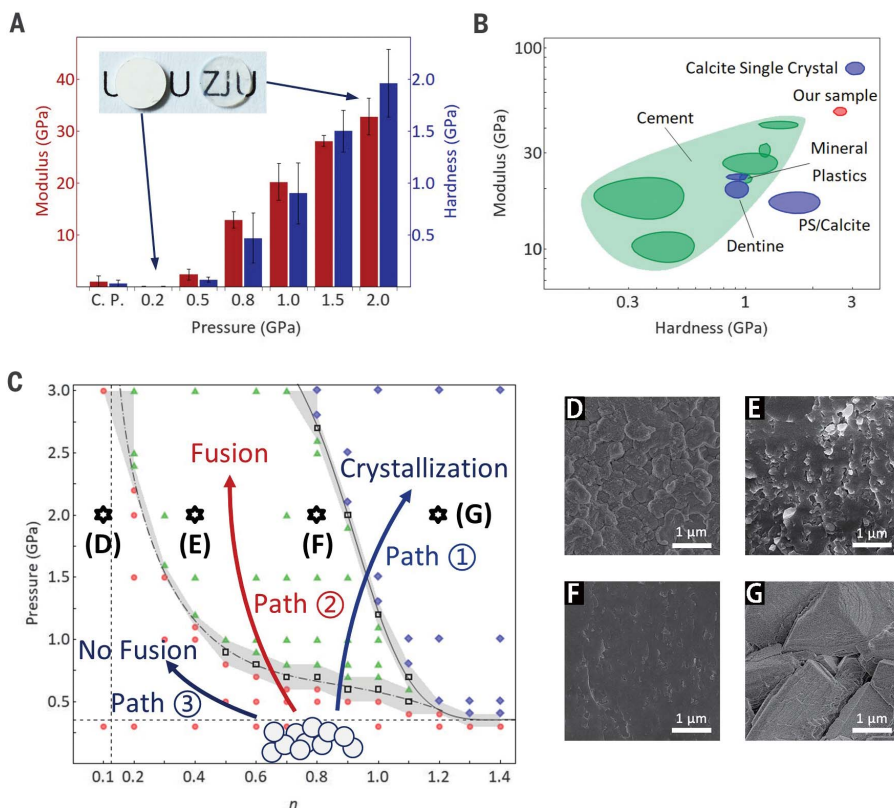


Fig. 2. Behaviors of particle fusion to bulks. (A) Nanoindentation tests of ACC bulks, which are obtained at different pressures from 0.2 to 2.0 GPa. C. P. represents pure calcite bulk, which is obtained from calcite particles at 2 GPa. Error bars indicate the SD of the average for more than five measurements. (Inset) Optical photos of the ACC bulks obtained under 0.2 and 2.0 GPa, respectively. The diameter of each ACC bulk is 4 mm. (B) Comparison of mechanical properties between prepared ACC bulks through coalescence of ACC particles (our sample) with other materials. PS/Calcite, calcite-filled polystyrene. (C) Phase diagram of ACC particles with different n under different pressures. Red circles, nonfusion conditions; green triangles, fusion conditions; blue rhombuses, crystallization conditions; black squares, conditions in which more than one phenomenon is detected. Gray regions represent the boundaries of fusion-nonfusion, fusion-crystallization, and nonfusion-crystallization areas. (D to G) SEM images of representative coalescence behaviors, corresponding to points (D) to (G) in panel (C).

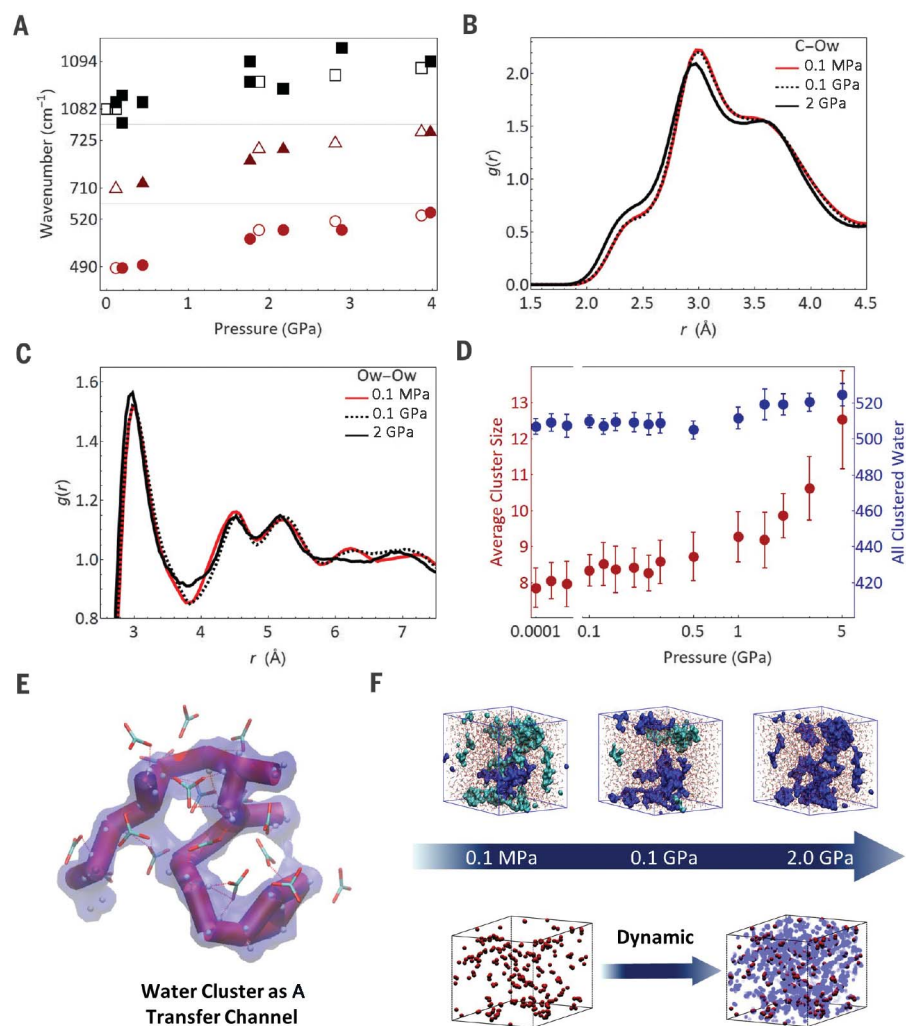


Fig. 3. Evolution of water clusters during pressure treatment. (A) Peak displacement of the in situ Raman spectrum in a compression-decompression process. Solid points and hollow points respectively represent compression and decompression processes. (B and C) PDFs [denoted by $g(r)$] of the C-Ow (carbon atom of carbonate-oxygen atom of water) and Ow-Ow pairs calculated according to simulations under different pressures. r , radius. (D) Changes in average water cluster size and total number of water clusters. The average water cluster size represents the average number of water molecules that are contained in clusters. "All clustered water" represents the total number of water molecules that form clusters. Error bars indicate the SD of the average for successive 5-ns data windows. (E) Illustration of a typical water cluster. (F) (Top) Illustration of the aggregation between clusters with increasing pressure. A main water cluster (blue) will gradually aggregate with other small clusters (cyan) to form a larger cluster. (Bottom) Illustration of the dynamic equilibration between clusters under pressure. Water in a cluster (red) will form new clusters (light blue) while disconnecting and reaggregating.

with $E = 0.100 \pm 0.020$ GPa and $H = 0.003 \pm 0.001$ GPa. At 2.0 GPa, E and H of the resulting material increased to 32.783 ± 3.537 GPa and 1.962 ± 0.327 GPa, respectively, which are substantially higher than those of the calcite bulk (fig. S9) constructed with calcite powder at the same P , which had E and H of 0.100 to 2.700 GPa and 0.010 to 0.040 GPa, respectively (Fig. 2A). In comparison with the original ACC particles, the monolith exhibited improved stability with increased kinetic persistence against crystallization (fig. S10), which is at-

tributed to its reduced specific surface area by particle fusion.

To provide a comprehensive understanding of the P -induced fusion of ACC with different n values, we generated a phase diagram of ACC from our collected data. The phase diagram shows three major zones of crystallization, fusion, and no fusion (Fig. 2C). The phase diagram reveals that both P and n have important effects on the behaviors of the ACC. At low P , the driving force is insufficient, so all primary ACCs with different n values

are neither fused nor crystallized. As P increases, the driving force becomes sufficient, and an effect of n exists. ACC takes different paths, depending on the value of n . ACC with abundant water ($n > 0.7$ to 1.2, which is related to P) is more likely to crystallize (path 1) to form calcite or vaterite (Fig. 2G). With decreasing n , P -induced coalescence (path 2) becomes increasingly favorable, which leads to particle-particle coalescence rather than crystallization ($n < 0.7$ to 1.2, which is related to P) (Fig. 2, E and F). However, sufficient water is important to maintain the shape stability of ACC. If n is less than ~ 0.1 , ACC neither coalesces nor crystallizes, but cracks under P (path 3 in Fig. 2D) and forms numerous tiny particles. The diagram shows that the synergistic effect of n and P is key to ensuring particle-particle fusion. Generally, n (the water in ACC) includes mobile and structural water (32). The thermogravimetric analysis curves indicate the domination of structural water when $n < 0.6$ (fig. S2D). Figure 2C shows that increasing the amount of either structural water ($n = 0.1$ to 0.6) or mobile water ($n = 0.6$ to 1.1) promotes the fusion process, because both are involved in the pressure-driven treatment. Furthermore, our Raman study implied a degenerate state of water under high pressure for fusion (fig. S11) (30). According to the phase diagram, both n and P can be further optimized, and the "best" ACC monolith was prepared under conditions of $n \approx 0.3$ and $P = 3.0$ GPa (the maximum P in our experiment), with E and H values of 49.673 ± 3.490 GPa and 2.739 ± 0.249 GPa, respectively (fig. S12). This fused ACC monolith is superior to many cements and calcium carbonate-based composites and is even similar to single-crystal calcite (Fig. 2B) (24).

We used in situ Raman spectroscopy of ACC at a high P and molecular simulation to understand P -driven coalescence and crystallization. The peak at ~ 712 cm⁻¹ in the Raman spectrum (fig. S13) corresponds to the in-plane bending (ν_4) of carbonate molecules. The peak had a blueshift and redshift during compression and pressure release, respectively (Fig. 3A). The same changes also appeared in two other peaks at 490 and 1082 cm⁻¹. In ACC, H bonds are considered the primary interaction between water and carbonate and result in a redshift in the C=O vibration frequency (29). The apparent blueshift with increasing P implies the weakening of these H bonds, which reflects dissociation between water and carbonates. This effect contributed to the loss of absorbed water (33) after the separation of H₂O and CO₃²⁻ in the ACC phase. With separation, water and ions aggregate to form water clusters, which provide migration channels to enhance mass transportation within ACC (34).

We employed a bulk phase of ACC to understand its internal ion transport with different

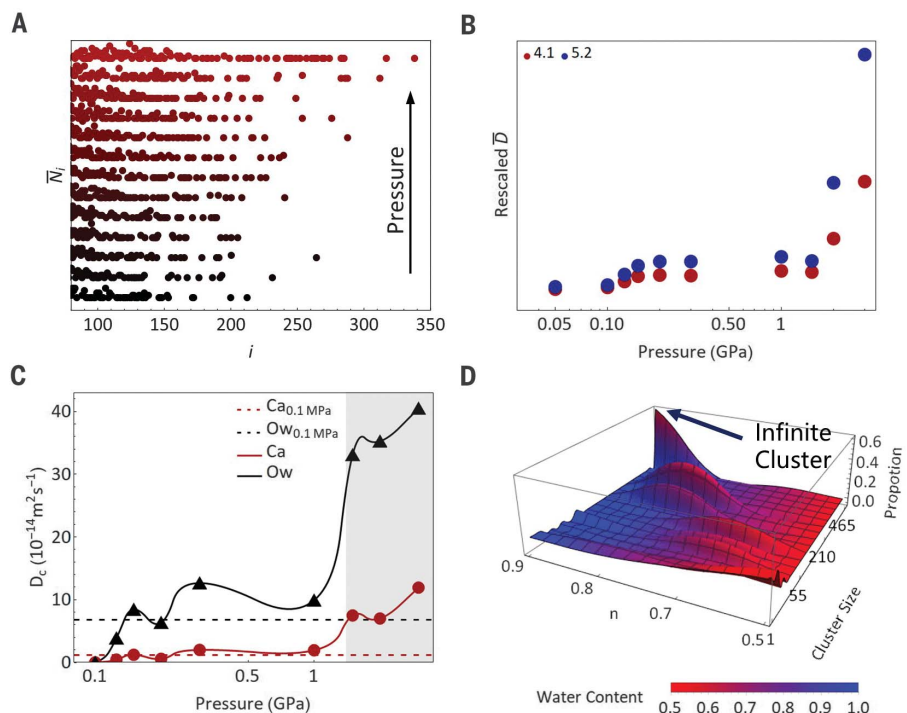


Fig. 4. Understandings of diffusivity in ACC. (A) \bar{N}_i becomes larger with increasing pressure. (B) Calculated diffusivity with increasing pressure, for $d = 4.1$ and 5.2 . (C) Diffusion coefficient D_c of water and Ca (calcium ions). The diffusion coefficient of carbonate is approximately equal to that of Ca. The gray area is where ACC particles fuse. (D) Distribution of water clusters directly affected by water content. The largest cluster is an infinite cluster throughout the whole system.

n and P values. The coordination environment, presented by pair distribution functions (PDFs), at 2 GPa is clearly different from those at lower P values (Fig. 3, B and C), indicating that diffusivity varies with pressure change. The structural changes reflected in the PDFs (Fig. 3, B and C, and fig. S14) verify the dissociation between water and carbonate and the aggregation of desorbed water from the carbonate, showing consistency between the Raman and simulation results. We can use percolation theory (35) for clusters to understand the relation between the structural change and diffusivity in a semiquantitative way. With aggregation, the changes in the scale and morphology of water clusters are substantial and act on mass transfer. We used 3.8 \AA as the cutoff distance to analyze water clusters (34). The calculation results intuitively reflect the aggregation of water, forming larger clusters (Fig. 3, D and E) under P . However, clusters exist under dynamic equilibrium (Fig. 3F and fig. S15) instead of as a localized framework so that clusters will disperse throughout the whole system with sufficient time. Moreover, the ability of mass transfer D for units in water clusters is related to the scale length λ_m (35), which is affected by the scale and the fractal dimension

$$D \propto D_0 \frac{\lambda_m^{2-H+1/\nu}}{\lambda_0^{1/\nu+H-2}} \quad (1)$$

where D_0 is the diffusivity of a single, unclustered water molecule; λ_0 is the unit size of water; and $H \in (-1/\nu, 0)$ and $\nu \approx 0.9$ are coefficients related to the fractal dimension of water clusters (35). The diffusivity of all water \bar{D} is the arithmetic mean of D

$$\bar{D} = \frac{\sum i N_i D_0 \lambda_i^{2-H_i+1/\nu_i} \lambda_0^{2-1/\nu_i-H_i}}{\sum i N_i} \quad (2)$$

where i is the number of molecules contained in a water cluster and N_i is the number of water clusters that contain i molecules. For all water clusters, λ_0 can be regarded as the same. D_0 as an intensive quantity can be affected by the coordination environment. Considering the maintenance of the ACC frame during pressing (fig. S13), D_0 is regarded as a constant, and the dominant factors that determine \bar{D} are scale and morphology. We employed two methods (34) to measure the fractal dimension of clusters, both of which show the invariance of the fractal dimension for large clusters (figs. S16 and S17). Because large clusters contribute much more than small clusters to \bar{D} (fig. S18), the fractal dimension is approximately considered to be the same for each cluster. Thus, λ_i can be substituted by i , and \bar{D} can be written as follows

$$\bar{D} \propto \frac{\sum i^d N_i}{\sum i N_i}, d = 3 - H_i + 1/\nu \quad (3)$$

where d is a coefficient with a value of 4.1 to 5.2 (considered constant during pressing). Because clusters exist in dynamic equilibrium, N_i is replaced by the time-averaged \bar{N}_i in statistical calculations. According to Eq. 3, molecules in a cluster that contains more molecules or has simpler morphology have stronger diffusivity. Specifically, these water molecules are less restrained by carbonates (36). As expected, N_i becomes larger along with P (Fig. 4A), and \bar{D} increases slowly until $P = 2.0$ GPa, then rises sharply with increasing P (Fig. 4B), whether near the lower bound of $d = 4.1$ or the upper bound of $d = 5.2$, consistent with another result calculated from the free path (Fig. 4C and fig. S19). This critical P at approximately $P = 1.0$ to 2.0 GPa is close to the boundary of the fusion and nonfusion areas in the phase diagram. Although the discussion above concerns water, it should be noted that the diffusivity of ions is correlated with water (Fig. 4C), owing to the interactions between ions and water. Strong water diffusion must be accompanied by corresponding strong ion diffusion in ACC (37, 38). From this analysis, we suggest that gradual aggregation leads to a qualitative change in the capacity of mass transportation for the whole system, finally leading to complete fusion.

Our results above could also be used to understand the role of water content in the experimental phase diagram. According to Eq. 3, the cluster distribution N_i apparently controls the diffusivity. N_i is directly determined by water content. For two types of ACCs with different n values of 0.5 and 0.7, the largest water cluster sizes are approximately 18 and 77 under ambient conditions. Considering the high order of i in Eq. 3, the gap in diffusivity is particularly evident and will widen under high P . This gap suggests why fusion is difficult to observe in areas with low water content. However, after n increases to approximately 0.8 to 0.9, a type of water cluster that expands the boundary of the simulation cell appears (Fig. 4D)—it is termed the infinite cluster (39). Typically (34), the critical condition of n for infinite clusters is independent of the simulation scale. The value of i of these infinite clusters is considered infinite; then, \bar{D} approaches infinity as well, which contradicts common sense. Actually, the infinite clusters exceed the domain of the definition applied for finite clusters in Eq. 1, so Eq. 3 becomes invalid. Any point of the solid can reach from the outside to within this kind of infinite cluster (40) to enable long-range mass transfer, which results in particle fusion as well as phase separation (crystallization). We note that $n = 0.8$ to 0.9 is close to the critical value of the phase diagram for different tendencies previously reported (34).

In our experiments, the fusion process of the pure ACC particles is independent of their sizes, synthesis methods, or pressing device

(opened or closed) for appropriate values of n (figs. S20, S2C, and S21) (30). However, humidity and temperature are the surrounding conditions that may affect the formation of monoliths as well as their structural uniformity and continuity, because the induced crystallizations are competitive with fusion (figs. S2A and S10) (30). Moreover, high temperature ($>50^{\circ}\text{C}$) can result in decreased n for the ACC samples (fig. S2D). Natural and many synthetic ACC samples contain additives (41, 42). Although fusion could proceed in the presence of additives such as Mg^{2+} , citrate, and polyacrylic acid, higher pressures were always required (fig. S22). The interactions between additives and water or ions (43–48) decrease their initial diffusion coefficients (30). Therefore, the control of additives is an approach to regulate pressure-induced fusion. The similar pressure-driven fusion of amorphous particles could be extended to other inorganic ionic compounds such as calcium phosphate and magnesium carbonate, demonstrating its general applicability (fig. S23).

This pressure-driven fusion through dynamic water channels provides a feasible method to achieve inorganic monoliths with optimized characteristics from their amorphous particles. Furthermore, the resulting monoliths can be used as conformable precursors for moldable preparation of crystalline materials by a shape- and mechanical strength-preserving solid-state crystallization (fig. S24) (49). Our preparation of a calcite bulk from the ACC particles is analogous to biomineralization of complete skeletons by using numerous amorphous particles.

Understanding the role of water channels promotes the mass transportation of solid inorganic particles, favoring the fusion of particle precursors for monolithic material construction. This approach is distinct from the classical sintering approach because high temperature is necessary in sintering to improve mass transportation, which is incompatible with thermally sensitive materials. Our findings focus on the internal structure of solid inorganic particles to improve mass

transportation, which is extremely suitable for the construction of most thermally sensitive materials, such as biominerals and biomaterials. This understanding establishes an alternative strategy for the construction of continuously structured materials, enabling large-scale and efficient manufacturing of inorganic monoliths.

REFERENCES AND NOTES

1. F. L. Riley, *J. Am. Ceram. Soc.* **83**, 245–265 (2000).
2. M. A. Meyers, P.-Y. Chen, A. Y.-M. Lin, Y. Seki, *Prog. Mater. Sci.* **53**, 1–206 (2008).
3. H. H. K. Xu *et al.*, *Bone Res.* **5**, 17056 (2017).
4. C. Hu, Z. Li, *Constr. Build. Mater.* **90**, 80–90 (2015).
5. N. T. K. Thanh, N. Maclean, S. Mahiddine, *Chem. Rev.* **114**, 7610–7630 (2014).
6. J. Guo *et al.*, *Angew. Chem. Int. Ed.* **55**, 11457–11461 (2016).
7. C. Wang *et al.*, *Science* **368**, 521–526 (2020).
8. H. Zhang, B.-N. Kim, K. Morita, H. Y. Keijiro Hiraga, Y. Sakka, *Sci. Technol. Adv. Mater.* **12**, 055003 (2011).
9. J. W. Evans, L. De Jonghe, Eds., in *The Production and Processing of Inorganic Materials* (Springer, 2016), pp. 383–439.
10. Z. Mu, R. Tang, Z. Liu, *Nanomaterials* **11**, 241 (2021).
11. J. Nowotny, T. Bak, T. Burg, M. K. Nowotny, L. R. Sheppard, *J. Phys. Chem. C* **111**, 9769–9778 (2007).
12. J. Salzman, C. Uzan-Saguy, B. Meyler, R. Kalish, *Phys. Stat. Sol. A* **176**, 683–687 (1999).
13. N. Ding, C.-M. L. Wu, H. Li, *Phys. Chem. Chem. Phys.* **16**, 23716–23722 (2014).
14. M. Albéric *et al.*, *Cryst. Growth Des.* **18**, 2189–2201 (2018).
15. J. R. Young *et al.*, *Rev. Mineral. Geochem.* **54**, 189–215 (2003).
16. L. Addadi, S. Weiner, *Phys. Scr.* **89**, 098003 (2014).
17. Y. Politi, T. Arad, E. Klein, S. Weiner, L. Addadi, *Science* **306**, 1161–1164 (2004).
18. J. Mahamid *et al.*, *Proc. Natl. Acad. Sci. U.S.A.* **107**, 6316–6321 (2010).
19. L. Yang, C. E. Killian, M. Kunz, N. Tamura, P. U. P. A. Gilbert, *Nanoscale* **3**, 603–609 (2011).
20. H. Du *et al.*, *Chem. Mater.* **32**, 4282–4291 (2020).
21. T. Yoshino, K. Maruyama, H. Kagi, M. Nara, J. C. Kim, *Cryst. Growth Des.* **12**, 3357–3361 (2012).
22. T. Mass *et al.*, *Proc. Natl. Acad. Sci. U.S.A.* **114**, E7670–E7678 (2017).
23. C. Y. Sun *et al.*, *Proc. Natl. Acad. Sci. U.S.A.* **117**, 30159–30170 (2020).
24. C. Merkel *et al.*, *J. Struct. Biol.* **168**, 396–408 (2009).
25. H. Du *et al.*, *J. Am. Chem. Soc.* **140**, 14289–14299 (2018).
26. A. V. Radha, T. Z. Forbes, C. E. Killian, P. U. P. A. Gilbert, A. Navrotsky, *Proc. Natl. Acad. Sci. U.S.A.* **107**, 16438–16443 (2010).
27. J. Bolze *et al.*, *Langmuir* **18**, 8364–8369 (2002).
28. J. Bolze, D. Pontoni, M. Ballauff, T. Narayanan, H. Cölfen, *J. Colloid Interface Sci.* **277**, 84–94 (2004).
29. A. Fernandez-Martinez, B. Kalkan, S. M. Clark, G. A. Waychunas, *Angew. Chem. Int. Ed.* **52**, 8354–8357 (2013).
30. Materials and methods are available as supplementary materials.
31. M. Saharay, A. O. Yazaydin, R. J. Kirkpatrick, *J. Phys. Chem. B* **117**, 3328–3336 (2013).

32. C. Günther, A. Becker, G. Wolf, M. Epple, *Z. Anorg. Allg. Chem.* **631**, 2830–2835 (2005).
33. S. A. Parry, A. R. Pawley, R. L. Jones, S. M. Clark, *Am. Mineral.* **92**, 525–531 (2007).
34. Y. G. Bushuev, A. R. Finney, P. M. Rodger, *Cryst. Growth Des.* **15**, 5269–5279 (2015).
35. M. B. Isichenko, *Rev. Mod. Phys.* **64**, 961–1043 (1992).
36. R. J. Reeder *et al.*, *Cryst. Growth Des.* **13**, 1905–1914 (2013).
37. A. C. S. Jensen *et al.*, *J. Phys. Chem. C* **122**, 3591–3598 (2018).
38. A. Koishi *et al.*, *J. Phys. Chem. C* **122**, 16983–16991 (2018).
39. A. Geiger, H. E. Stanley, *Phys. Rev. Lett.* **49**, 1895–1898 (1982).
40. M. Rosso, J. F. Gouyet, B. Sapoval, *Phys. Rev. Lett.* **57**, 3195–3198 (1986).
41. F. C. Meldrum, H. Cölfen, *Chem. Rev.* **108**, 4332–4432 (2008).
42. S. Weiner, Y. Levi-Kalishman, S. Raz, L. Addadi, *Connect. Tissue Res.* **44** (suppl. 1), 214–218 (2003).
43. E. Loste, R. M. Wilson, R. Seshadri, F. C. Meldrum, *J. Cryst. Growth* **254**, 206–218 (2003).
44. S. Raz, S. Weiner, L. Addadi, *Adv. Mater.* **12**, 38–42 (2000).
45. F. Lippmann, in *Sedimentary Carbonate Minerals* (Springer, 1973), p. 79.
46. D. Gebauer, H. Cölfen, A. Verch, M. Antonietti, *Adv. Mater.* **21**, 435–439 (2009).
47. D. J. Tobler *et al.*, *Adv. Funct. Mater.* **25**, 3081–3090 (2015).
48. X.-R. Xu *et al.*, *J. Cryst. Growth* **310**, 3779–3787 (2008).
49. Z. Liu *et al.*, *Nature* **574**, 394–398 (2019).

ACKNOWLEDGMENTS

We thank J. J. De Yoreo for discussions, L. Zhang for assistance with synchrotron XRD at the Shanghai Synchrotron Radiation Facility, and F. Chen for assistance with electron microscopy. **Funding:** The authors acknowledge funding support from the National Natural Science Foundation of China (21625105, 22022511, 21805241, and 61805081), the National Key Research and Development Program of China (2020YFA0710400), and the Fundamental Research Funds for the Central Universities (2021FZZX001-04). **Author contributions:** Z.L. and R.T. initiated the project. Z.M. synthesized all samples and performed most examinations. K.K. performed the simulation. Z.M., K.K., K.J., and H.D. together acquired and analyzed the synchrotron XRD data. Z.M. and K.J. acquired in situ high-pressure Raman spectroscopy data; Z.M., K.K., and X.X. analyzed these data. Z.M., K.K., Z.L., and R.T. wrote the manuscript and compiled the figures. All authors discussed the results and provided feedback on the manuscript. **Competing interests:** The authors declare no competing interests. **Data and materials availability:** All data are available in the main text or the supplementary materials.

SUPPLEMENTARY MATERIALS

science.sciencemag.org/content/372/6549/1466/suppl/DC1
Materials and Methods
Supplementary Text
Figs. S1 to S28
References (50–68)

16 December 2020; accepted 18 May 2021
10.1126/science.abg1915

Pressure-driven fusion of amorphous particles into integrated monoliths

Zhao Mu, Kangren Kong, Kai Jiang, Hongliang Dong, Xurong Xu, Zhaoming Liu and Ruikang Tang

Science **372** (6549), 1466-1470.

DOI: 10.1126/science.abg1915

The making of a monolith

Amorphous calcium carbonate is a hard material that is difficult to make into large, clear blocks. It is also sensitive to heating, and compacting the starting nanoparticles too much tends to lead to crystallization. Mu *et al.* determined the optimal amount of water in amorphous calcium carbonate to create clear, solid monoliths through compression. The key is to regulate the amount of diffusion in the system so that particle boundaries fuse without triggering sample-wide crystallization. This fusion strategy may also work for similar amorphous inorganic ionic compounds.

Science, abg1915, this issue p. 1466

ARTICLE TOOLS

<http://science.sciencemag.org/content/372/6549/1466>

SUPPLEMENTARY MATERIALS

<http://science.sciencemag.org/content/suppl/2021/06/23/372.6549.1466.DC1>

REFERENCES

This article cites 66 articles, 9 of which you can access for free
<http://science.sciencemag.org/content/372/6549/1466#BIBL>

PERMISSIONS

<http://www.sciencemag.org/help/reprints-and-permissions>

Use of this article is subject to the [Terms of Service](#)

Science (print ISSN 0036-8075; online ISSN 1095-9203) is published by the American Association for the Advancement of Science, 1200 New York Avenue NW, Washington, DC 20005. The title *Science* is a registered trademark of AAAS.

Copyright © 2021 The Authors, some rights reserved; exclusive licensee American Association for the Advancement of Science. No claim to original U.S. Government Works